Research Article

Dynamic Topology Optimization of Constrained Damping Plates considering Frequency and Temperature Characteristics Based on an Efficient Strategy

Fan Wu (ID) **and Pu Xue** (ID)

School of Aeronautics, Northwestern Polytechnical University, Youyi West Road, Xian 710002, Shaanxi, China

Correspondence should be addressed to Pu Xue; p.xue@nwpu.edu.cn

The frequency- and temperature-dependent characteristics of viscoelastic materials significantly affect the vibration response of the damped composite structures. In this paper, an efficient strategy of hybrid expansion combined with dynamic reduction is developed to solve the steady-state response of the frequency- and temperature-dependent viscoelastic structure characterized by nonproportional system, and the sensitivity analysis is carried out based on the adjoint variable method. The similarity index is defined to distinguish the correlation among different design layouts. Two instances demonstrated the validity of the proposed approach. The findings indicated that a positive compromise between accuracy and efficiency can be achieved, and the computational time can be significantly reduced while ensuring the accuracy of the results. Furthermore, it has been discovered that the excitation frequency and temperature significantly impact the optimal configuration of damping material. The effects of layer thicknesses and volume fractions on optimization designs are also further investigated.

1. Introduction

Thin-walled constructions are frequently utilized as load-bearing components in autos, railways, ships, space shuttles, and other engineering structures. Due to the growing desire for lightweight design, these structures are prone to severe vibration and noise concerns when subjected to external dynamic excitations. Passive control treatments, such as incorporating viscoelastic damping materials into structures, were generally regarded as a practical and effective technique to suppress the level of vibration in structures [1–3]. Since the 1960s, constrained layer damping (CLD) structures have been widely used in vibration control of aerospace structures due to their substantially higher energy dissipation on account of shear deformation than free layer damping. Various CLD structures have emerged as hot topics and trends, with key research focusing on dynamic modeling and analysis [3, 4], performance identification [5, 6], position optimization, and viscoelastic material parametric design.

Topology optimization technology has been widely applied in the conceptual design of the optimal layout of damping materials due to its effectiveness, aiming to achieve greater performance in decreasing vibration and abating noise under lightweight constraints. In the field of dynamic characteristics, fundamental or multiple modal loss factors are frequently employed as objective functions. Zheng et al. [7] investigated the structural design configuration using the genetic algorithm for minimizing the overall vibration energy. Wang et al. [8] proposed an artificial density and heuristic methods for optimization design of CLD shells. Kim et al. [9] optimize the distribution of damping materials by maximizing the structural modal loss factor. Xu et al. [10] applied topology design technology to estimate the material distribution in the spindle box of machine tools to increase vibration suppression ability. Recently, Zhang et al. [11] investigated the topology optimization of multiphase viscoelastic microstructures to enhance macroscopic damping performance. For dynamic response optimization, many notable works have been carried out to

suppress the structural vibration. Fang et al. [12] adopted the density-based method to reduce the structural dynamic response. Zheng et al. [13] discussed the topological optimization of CLD structures to minimize sound radiation. Takezawa [14] took the complex dynamic compliance as a novel objective function to lessen the resonant response by maximizing the energy dissipation near the resonance. Delissen et al. [15] proposed a constraint function based on enhanced modal truncation to limit the frequency response peak at the resonance using an efficient reduced-order model. Furthermore, Kang et al. [16, 17] adopted the classical Rayleigh damping model to describe the energy dissipation of viscoelastic materials and found that the specific design configurations are sensitive to the damping coefficients. Nevertheless, the frequency- and temperature-dependent properties of viscoelastic materials are still rarely considered in the optimization design of viscoelastic structures, and the corresponding difficulties and challenges have not been well addressed.

It should be emphasized that the dynamic mechanical properties of viscoelastic materials are affected by the coupling of several factors, the most relevant of which are the temperature and frequency [6, 18, 19]. The following lists some recent meaningful work. Li et al. [20] investigated the vibrations of composite structures subjected to partial CLD treatment by using the strain-dependent shear modulus. Oh [21] investigated the damping performance of laminated shells considering the frequency and temperature dependence. Shu et al. [22] established an accurate dynamic equation of CLD structure and analyzed its vibration characteristics using the coupling effect of temperature and frequency. Mokhtari et al. [23] quantitatively analyzed the dynamic response and behavior of viscoelastic layers in CLD cylindrical shells. Sun et al. [24] conducted a thorough examination and discussion of the effect of frequency on the vibration behavior of composite structures. Dai et al. [25] then investigated the damping performance of laminated shells with frequency-dependent properties and derived the analytical expression of dynamic response. These published works all concur with the conclusion that the viscoelastic materials' frequency and temperature dependence are essential when evaluating the dynamic response and damping behavior of CLD structures.

As far as the authors know, despite the fact that dynamic topology optimization of CLD structures has been extensively and thoroughly researched, few research reports address the difficulties of optimizing the design of viscoelastic structures. Recently, Zhang et al. [26] performed the topology optimization study for maximizing the modal loss factor of the CLD structure considering temperature and frequency dependence by means of a parametric level set method based on the generalized Maxwell model. However, their work did not involve attenuating the structural response. As a result, the originality of this study is primarily reflected in the efficient optimization design approach which aims to reduce the dynamic response of viscoelastic structural materials comprising the frequency- and temperature-dependent damping materials. Therefore, the application scope of Golla–Hughes–McTavish (GHM) model [27, 28] is extended to solve the optimal layout problem of the CLD plate. However, this composite structure is characterized by

nonproportional damping system owing to the nonuniform distribution of viscoelastic materials. Recently, Li et al. [29] proposed an N-space approach to correct the higher-order responses using the established relationship between the eigensolutions and the system matrix. These findings provide the potential to be a driving factor in the application and popularization of the nonproportional damped systems in the field of topology optimization.

The aim of this paper is to study the topology optimization design of viscoelastic composite structures at different temperatures and frequencies to minimize the steady-state response. For this purpose, the GHM model was incorporated into the finite element method to describe the energy dissipation of materials. To handle the topology optimization difficulties characterized by nonproportional damping of the CLD plate resulting from this, an improved approach integrating hybrid expansion and dynamic reduction methods is proposed and developed, and the sensitivity analysis of adjoint schemes is performed. Specific attention focuses on the influence of the fluctuation of viscoelastic material properties with the change of temperature and frequency on the vibration response and optimal configuration of composite structures.

The remainder of the paper was structured as follows. Section 2 established the augmented vibration equations incorporating the GHM model, taking into account the frequency- and temperature-dependent properties of viscoelastic materials. Section 3 described the specific procedure for calculating the displacement response of CLD plates under harmonic excitations by combining hybrid expansion and dynamic reduction methods. The formulations of topology optimization of CLD plate and sensitivity analysis based on the adjoint variable method (AVM) are reviewed in Section 4. In section 5, several numerical examples are implemented to validate the proposed optimization method and evaluated the effects of frequency and temperature on the optimal layouts. Besides, the influence of the layer thicknesses and volume fractions is also further discussed. Conclusions are drawn in section 6.

2. Numerical Modeling Procedure

The CLD plates, as a king of common multilayer structures, are extensively applied in many engineering fields. This section presents the related theories for the numerical modeling procedure of CLD plates incorporating the GHM model.

2.1. Basic Kinetics Relationships. Figure 1 depicts a schematic illustration of the CLD plate. The symbol h represents the thickness, while the subscripts p, c, and v, respectively, denote the base plate, constrained layer, and damping layer. The coordinate system is set on the neutral plane of the CLD plates, and the position of the neutral axis can be obtained by balancing the forces in the out-of-plane direction.

Considering the dynamic deformations, as shown in Figure 1, the midplane displacements u_v and v_v and the shear strains β_x and β_y are given as
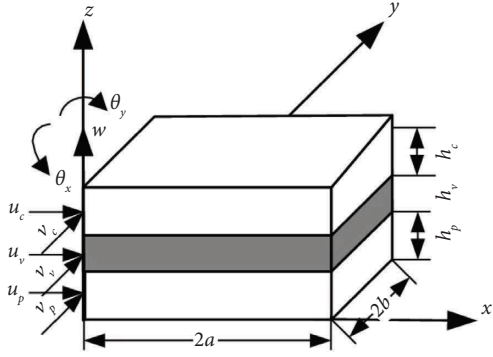
Figure 1: Schematic diagram of the CLD plate.

$$u_v = \frac{1}{2}\left[(u_c + u_p) + \frac{h_c - h_p}{2}\theta x\right],$$

$$v_v = \frac{1}{2}\left[(v_c + v_p) + \frac{h_c - h_p}{2}\theta y\right], \tag{1}$$

$$\beta_x = \frac{u_c - u_p}{h_v} + \frac{d}{h_v}\theta_x,$$

$$\beta_y = \frac{v_c - v_p}{h_v} + \frac{d}{h_v}\theta_y, \tag{2}$$

where u_c and v_c and u_p and v_p denote midplane displacements of constrained layer and base plate, respectively. w is the out-of-plane displacement, $\theta_x = \partial w/\partial x$ and $\theta_y = \partial w/\partial y$ denote the partial derivatives of w in x and y directions, and $d = h_v + (h_c + h_p)/2$ is the midplanes distance.

2.2. Finite Element Models.
The finite element model is discreted into four-node planar plate element, and the nodal displacement vector is determined by

$$\mathbf{q}^e = \{\mathbf{q}_1^e \ \mathbf{q}_2^e \ \mathbf{q}_3^e \ \mathbf{q}_4^e\}^{\mathrm{T}}, \tag{3}$$

in which

$$\mathbf{q}_i^e = \{u_{ci} \ v_{ci} \ u_{pi} \ v_{pi} \ w_i \ \theta_{xi} \ \theta_{yi}\}, \quad \text{for } i = 1, 2, 3, 4. \tag{4}$$

Therefore, the displacement at any position within the element can be represented by the node displacement as follows:

$$\begin{aligned}&\{u_c \ v_c \ u_p \ v_p \ w \ \theta_x \ \theta_y\}^{\mathrm{T}}\\&= \{\mathbf{N}_{uc} \ \mathbf{N}_{vc} \ \mathbf{N}_{up} \ \mathbf{N}_{vp} \ \mathbf{N}_w \ \mathbf{N}_{\theta x} \ \mathbf{N}_{\theta y}\}\mathbf{q}^e,\end{aligned} \tag{5}$$

where $\mathbf{N}_{uc}$, $\mathbf{N}_{vc}$, $\mathbf{N}_{up}$, $\mathbf{N}_{vp}$, $\mathbf{N}_w$, $\mathbf{N}_{\theta x}$, and $\mathbf{N}_{\theta y}$ are the spatial interpolating vectors corresponding to u_c, v_c, u_p, v_p, w, θ_x, and θ_y, respectively.

In addition, the spatial interpolating vectors corresponding to u_v, v_v, β_x, and β_y can be derived from (1) and (2), given as

$$\mathbf{N}_{uv} = \frac{1}{2}\left[(\mathbf{N}_{uc} + \mathbf{N}_{up}) + \frac{h_c - h_p}{2}\mathbf{N}_{\theta x}\right],$$

$$\mathbf{N}_{vv} = \frac{1}{2}\left[(\mathbf{N}_{vc} + \mathbf{N}_{vp}) + \frac{h_c - h_p}{2}\mathbf{N}_{\theta y}\right],$$

$$\mathbf{N}_{\beta x} = \frac{1}{h_v}\left[(\mathbf{N}_{uc} - \mathbf{N}_{up}) + d\mathbf{N}_{\theta x}\right], \tag{6}$$

$$\mathbf{N}_{\beta x} = \frac{1}{h_v}\left[(\mathbf{N}_{vc} - \mathbf{N}_{vp}) + d\mathbf{N}_{\theta y}\right].$$

Then, the elemental mass and stiffness matrices can be obtained according to the energy approach and variational Hamilton principle as follows:

$$\mathbf{m}_i^e = \rho_i h_i \int_{-a}^{a}\int_{-b}^{b}\left[(\mathbf{N}_{ui})^{\mathrm{T}}\mathbf{N}_{ui} + (\mathbf{N}_{vi})^{\mathrm{T}}\mathbf{N}_{vi} + (\mathbf{N}_w)^{\mathrm{T}}\mathbf{N}_w\right]\mathrm{d}x\,\mathrm{d}y,$$

$$\mathbf{k}_i^e = h_i\int_{-a}^{a}\int_{-b}^{b}\mathbf{B}_{1i}^{\mathrm{T}}\mathbf{D}_i\mathbf{B}_{1i}\mathrm{d}x\,\mathrm{d}y + \frac{h_i^3}{12}\int_{-a}^{a}\int_{-b}^{b}\mathbf{B}_2^{\mathrm{T}}\mathbf{D}_i\mathbf{B}_2\mathrm{d}x\,\mathrm{d}y,$$

$$\mathbf{k}_{sv}^e = G_v h_v\int_{-a}^{a}\int_{-b}^{b}\left[(\mathbf{N}_{\beta x})^{\mathrm{T}}\mathbf{N}_{\beta x} + (\mathbf{N}_{\beta y})^{\mathrm{T}}\mathbf{N}_{\beta y}\right]\mathrm{d}x\,\mathrm{d}y, \tag{7}$$

where $\mathbf{k}_{sv}^e$ denotes the shear stiffness, $\mathbf{D}_i$ identifies the elastic matrix, and strain matrices are presented as

$$\mathbf{B}_{1i} = \left[\frac{\partial\mathbf{N}_{ui}}{\partial x} \ \frac{\partial\mathbf{N}_{vi}}{\partial y} \ \frac{\partial\mathbf{N}_{ui}}{\partial y} + \frac{\partial\mathbf{N}_{vi}}{\partial x}\right]^{\mathrm{T}},$$

$$\mathbf{B}_2 = \left[\frac{\partial^2\mathbf{N}_w}{\partial x^2} \ \frac{\partial^2\mathbf{N}_w}{\partial y^2} \ \frac{\partial^2\mathbf{N}_w}{\partial x\partial y}\right]^{\mathrm{T}}. \tag{8}$$

The elemental dynamic equation of composite structures is given as

$$\mathbf{m}^e\ddot{\mathbf{q}}^e + \mathbf{k}^e\mathbf{q}^e + \mathbf{k}_{sv}^e\mathbf{q}^e = \mathbf{f}, \tag{9}$$

where $\mathbf{m}^e = \mathbf{m}_p^e + \mathbf{m}_c^e + \mathbf{m}_v^e$ and $\mathbf{k}^e = \mathbf{k}_p^e + \mathbf{k}_c^e + \mathbf{k}_v^e$. $\mathbf{m}^e$ and $\mathbf{k}^e$ represent the composite elemental mass and stiffness matrixes, respectively.

2.3. Incorporation of Viscoelastic Materials.
For the CLD structures comprising viscoelastic material, equation (9) cannot capture their frequency-dependence. Hence, Golla–Hughes and McTavish [27, 28] introduced the GHM model to describe the energy dissipation of viscoelastic structures and expressed it in the following form:

$$s\widetilde{G}(s) = G^{\infty}\left[1 + \sum_{k=1}^{r}\alpha_k\frac{s^2 + 2\widehat{\zeta}_k\widehat{\omega}_k s}{s^2 + 2\widehat{\zeta}_k\widehat{\omega}_k + \widehat{\omega}_k^2}\right], \tag{10}$$

where G^{∞} is the equilibrium value of modulus. Each term includes α_k, $\widehat{\zeta}_k$, and $\widehat{\omega}_k$, which are determined via $G_v^*(\omega)$ at temperature T (°C). The number of mini-oscillator terms r could be adjusted to reflect the corresponding damping performance of different viscoelastic materials.

The Laplace's transform of (9) is

$$\left(s^2 \mathbf{m}^e + \mathbf{k}^e + s\widetilde{G}(s)\mathbf{k}^e_{sv}\right)\mathbf{q}^e(s) = \mathbf{f}(s). \tag{11}$$

Substituting (10) into (11) and introducing auxiliary coordinates called dissipation coordinates are defined as follows:

$$\mathbf{z}(s) = \frac{\widehat{\omega}^2}{s^2 + 2\widehat{\zeta}\omega s + \widehat{\omega}^2}\mathbf{q}^e(s). \tag{12}$$

Equation (9) is converted into the time domain and rewritten as follows:

$$\begin{bmatrix} \widehat{\mathbf{m}} & \widehat{\mathbf{m}}_z \end{bmatrix}\begin{bmatrix} \ddot{\mathbf{q}}^e \\ \ddot{\mathbf{z}} \end{bmatrix} + \begin{bmatrix} \widehat{\mathbf{c}} & \widehat{\mathbf{c}}_z \end{bmatrix}\begin{bmatrix} \dot{\mathbf{q}}^e \\ \dot{\mathbf{z}} \end{bmatrix} + \begin{bmatrix} \widehat{\mathbf{k}} & \widehat{\mathbf{k}}_z \end{bmatrix}\begin{bmatrix} \mathbf{q}^e \\ \mathbf{z} \end{bmatrix} = \begin{bmatrix} \mathbf{f} \\ \mathbf{0} \end{bmatrix}, \tag{13}$$

where

$$\widehat{\mathbf{m}} = \begin{bmatrix} \mathbf{m}^e \\ 0 \\ \vdots \\ 0 \end{bmatrix},$$

$$\widehat{\mathbf{m}}_z = \begin{bmatrix} 0 & \cdots & & 0 \\ \alpha_1\frac{1}{\widehat{\omega}_1^2}\Lambda & \ddots & & \vdots \\ 0 & & \ddots & 0 \\ 0 & & \cdots & \alpha_r\frac{1}{\widehat{\omega}_r^2}\Lambda \end{bmatrix},$$

$$\widehat{\mathbf{c}} = \begin{bmatrix} \mathbf{c}^e \\ 0 \\ \vdots \\ 0 \end{bmatrix},$$

$$\widehat{\mathbf{c}}_z = \begin{bmatrix} 0 & \cdots & & 0 \\ \alpha_1\frac{2\widehat{\zeta}_1}{\widehat{\omega}_1}\Lambda & \ddots & & \vdots \\ 0 & & \ddots & 0 \\ 0 & & \cdots & \alpha_r\frac{2\widehat{\zeta}_r}{\widehat{\omega}_r}\Lambda \end{bmatrix}, \tag{14}$$

$$\widehat{\mathbf{k}} = \begin{bmatrix} \mathbf{k}^e + \widetilde{\mathbf{k}}\left(1 + \sum_{k=1}^{r}\alpha_k\right) \\ -\alpha_1\mathbf{R}^{\mathrm{T}} \\ \vdots \\ -\alpha_r\mathbf{R}^{\mathrm{T}} \end{bmatrix},$$

$$\widehat{\mathbf{k}}_z = \begin{bmatrix} -\alpha_1\mathbf{R} & \cdots & -\alpha_r\mathbf{R} \\ \alpha_1\Lambda & 0 & 0 \\ 0 & \ddots & 0 \\ 0 & 0 & \alpha_r\Lambda \end{bmatrix},$$

$$\widetilde{\mathbf{k}} = G^{\infty}\mathbf{k}^e_{sv},$$

$$\mathbf{k}^e_{sv} = \mathbf{R}_v\Lambda_v\mathbf{R}^{\mathrm{T}}_v,$$

$$\Lambda = G^{\infty}\Lambda_v,$$

$$\mathbf{R} = \mathbf{R}_v\Lambda,$$

$$\mathbf{z} = \mathbf{R}^{\mathrm{T}}_v\widehat{\mathbf{z}}, \quad k = 1, 2, 3, \ldots, r,$$

where Λ_v is a diagonal matrix composed of the positive eigenvalues of the shear stiffness matrix of viscoelastic materials and $\mathbf{R}^{\mathrm{T}}_v$ is the matrix composed of the corresponding eigenvectors.

Each element can be considered to be composed of five nodes, four of which are physical and the other one is virtual. Each physical node has seven DOFs, and the introduced auxiliary coordinates are regarded as the DOFs of the corresponding virtual nodes, which are jointly determined by the number of positive eigenvalues and the orders of the mini-oscillators terms. Figure 2 presents the schematic diagram of the element nodes and assembly process of the global matrices.

The global matrices are assembled based on the physical coordinates while reserving auxiliary coordinates. The equation of motion is shown as follows:

$$\mathbf{M}\ddot{\mathbf{x}} + \mathbf{C}\dot{\mathbf{x}} + \mathbf{K}\mathbf{x} = \mathbf{F}, \tag{15}$$

where $\mathbf{M} \in \mathbf{R}^{N_G \times N_G}$, $\mathbf{K} \in \mathbf{R}^{N_G \times N_G}$, and $\mathbf{C} \in \mathbf{R}^{N_G \times N_G}$, respectively, denote the global mass, stiffness, and damping matrices. $\mathbf{x}$ and $\mathbf{F} \in \mathbf{R}^{N_G \times 1}$ represent the displacement vector and external load vector. Here, N_G indicates the full DOFs consisting of physical and dissipative coordinates.

The finite element method (FEM) provides a carrier for the fusion of the GHM model, so that the properties of viscoelastic materials can be introduced into the equation of motion of the structure in the form of the element mass, stiffness, and damping matrix. The dynamic equation obtained by this modeling method is a standard second-order linear system model, which performs well in response and sensitivity analysis.

3. Solutions of the Governing Equation

As previously stated, dissipative coordinates appear as the augmented state variables, significantly increasing the dimension of the governing equation. As a result of this, such a method suffers from the finite element dimension system being extended twice or more, necessitating expensive computing costs. Meanwhile, owing to the nonuniform design layouts of damping material, the composite structure represents the nonproportional damping behavior. Solving the governing equation directly is a computationally expensive task. Therefore, model reduction is necessary to reduce the high-order finite element models to a smaller size for undertaking more efficient dynamic analysis and optimization procedures.

3.1. Dynamic Reduction Method. The dynamic reduction method pioneered by Leung [30] and afterward Petersmann [31] as a type of hybrid coordinates reduction method is frequently and widely employed. This method employs the modal synthesis in conjunction with the dynamic reduction, which is analogous to the substructuring technique. According to the master and slave DOFs, the structural displacement vector can be separated into two subvectors. The displacement subvector of slave DOFs can be obtained as follows:
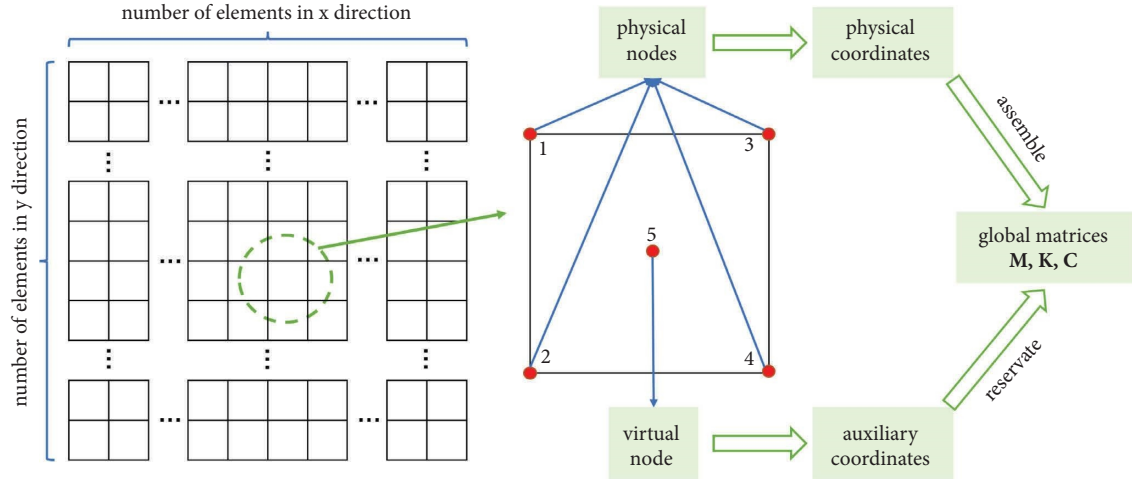
FIGURE 2: Schematic diagram of element nodes and assembly process.

$$\mathbf{q}^s = -\left(\mathbf{K}_q^{ss}\right)^{-1} \mathbf{K}_q^{sm} \mathbf{q}^m - \left(\mathbf{K}_q^{ss}\right)^{-1} \left[\mathbf{K}_{qz}^{sm} \mathbf{K}_{qz}^{ss}\right] \mathbf{z} + \mathbf{\Phi c}. \quad (16)$$

Rewrite (16) into matrix form as follows:

$$\begin{Bmatrix} \mathbf{q}^m \\ \mathbf{q}^s \\ \mathbf{z} \end{Bmatrix} = \underbrace{\begin{bmatrix} \mathbf{I}_1 & \mathbf{0} & \mathbf{0} \\ \mathbf{t}_1 & \mathbf{t}_2 & \mathbf{\Phi} \\ \mathbf{0} & \mathbf{I}_2 & \mathbf{0} \end{bmatrix}}_{\mathbf{T}} \begin{Bmatrix} \mathbf{q}^m \\ \mathbf{z} \\ \mathbf{c} \end{Bmatrix}, \quad (17)$$

where $\mathbf{T} \in \mathbf{R}^{N_G \times N_R}$ is the transformation matrix, $N_R \ll N_G$; $\mathbf{I}_1$ and $\mathbf{I}_2$ are the unit matrix; $\mathbf{t}_1 = -\left(\mathbf{K}_q^{ss}\right)^{-1} \mathbf{K}_q^{sm}$; and $\mathbf{t}_2 = -\left(\mathbf{K}_q^{ss}\right)^{-1} \left[\mathbf{K}_{qz}^{sm} \mathbf{K}_{qz}^{ss}\right]$ denote the static contribution, and $\mathbf{\Phi}$ represents the corresponding dynamic contribution.

Therefore, the reduced-space governing equation is showed as follows:

$$\left(\mathbf{T}^T \mathbf{M} \mathbf{T}\right) \ddot{\mathbf{y}} + \left(\mathbf{T}^T \mathbf{C} \mathbf{T}\right) \dot{\mathbf{y}} + \left(\mathbf{T}^T \mathbf{K} \mathbf{T}\right) \mathbf{y} = \mathbf{T}^T \mathbf{F}, \quad (18)$$

where $\mathbf{M}_{N_R} = \mathbf{T}^T \mathbf{M} \mathbf{T}$, $\mathbf{K}_{N_R} = \mathbf{T}^T \mathbf{K} \mathbf{T}$, $\mathbf{C}_{N_R} = \mathbf{T}^T \mathbf{C} \mathbf{T}$, and $\mathbf{F}_{N_R} = \mathbf{T}^T \mathbf{F}$, respectively, denote the reduced mass, stiffness, damping matrices, and load vector. Furthermore, please see [32] for the specific theories and the derivation of corresponding reduction space.

3.2. Complex Mode Superposition Method for Higher-Order Modes Correction.
The dynamic equation in the frequency domain of reduced order for the CLD structure with n_R DOFs can be expressed as follows:

$$\left(-\omega^2 \mathbf{M}_{N_R} + j\omega \mathbf{C}_{N_R} + \mathbf{K}_{N_R}\right) \mathbf{Y}(\omega) = \mathbf{K}_d(\omega) \mathbf{Y}(\omega) = \mathbf{F}_{N_R}(\omega), \quad (19)$$

where the matrix $\mathbf{K}_d(\omega) = -\omega^2 \mathbf{M}_{N_R} + j\omega \mathbf{C}_{N_R} + \mathbf{K}_{N_R}$ is the dynamic stiffness matrix and ω refers to the exciting frequency.

The complex frequency response function (FRF) matrix can be expressed using complex mode superposition theory, as shown as follows:

$$\mathbf{H}(\omega) = \sum_{i=1}^{2N_R} \frac{\phi_\mathbf{i} \phi_\mathbf{i}^T}{\mathbf{a}_\mathbf{i}\left(j\omega - \lambda_i\right)}, \quad (20)$$

where

$$\mathbf{a}_\mathbf{i} = \phi_\mathbf{i}^T\left(2\lambda_i \mathbf{M}_{N_R} + \mathbf{C}_{N_R}\right)\phi_\mathbf{i}, \quad (21)$$

where ϕ_r is the complex eigenvector that corresponds to the complex eigenvalue λ_r. We suppose that the complex eigenvalues are distinct and the number is $2 N_R$. In practice, only limited low-order modes can be involved.

$$\mathbf{H}(\omega) \approx \sum_{i=1}^L \frac{\phi_i^{T\phi_i}}{\left(j\omega - \lambda_i\right)\mathbf{a}_\mathbf{i}},$$

$$\mathbf{X}(\omega) \approx \sum_{i=1}^L \frac{\phi_i^T \mathbf{F}_{N_R}(\omega)\phi_i}{\left(j\omega - \lambda_i\right)\mathbf{a}_i}. \quad (22)$$

Equation (22) is the modal displacement method (MDM). The modal truncation error may be generated because some higher-order modes are disregarded. When $L \ll 2N_R$, the calculation results are hardly credible.

According to the method proposed by Li et al. [29], (20) is rewritten as the matrix form, and expanded the inverse term using the Neumann series as follows:

$$\mathbf{H}(\omega) = -\sum_{r=1}^\infty (j\omega)^{r-1} \mathbf{\Phi} \mathbf{\Theta}^{-1} \mathbf{\Lambda}^{-1} \mathbf{\Phi}^T, \quad (23)$$

where $\mathbf{\Lambda} = \text{diag}\left[\lambda_1, \lambda_2, \cdots, \lambda_{2N_R}\right]$, $\mathbf{\Phi} = \left[\boldsymbol{\varphi}_1, \boldsymbol{\varphi}_2, \cdots, \boldsymbol{\varphi}_{2N_R}\right]$, $\mathbf{\Theta} = \text{diag}\left[\mathbf{a}_1, \mathbf{a}_2, \cdots, \mathbf{a}_{2N_R}\right]$.

It should be noted that (23) can achieve the expected accuracy as long as all corresponding modes whose resonance frequency is within the concerned frequency interval are retained. It can be further proved that the series expansion in (23) is convergent.

The $\mathbf{K}_d(\omega)$ can be reformed and the inverse calculated as follows:

$$\mathbf{K}_d^{-1}(\omega) = \left[\mathbf{I}_{N_R} + j\omega\mathbf{K}_{N_R}^{-1}\left(\mathbf{C}_{N_R} + j\omega\mathbf{M}_{N_R}\right)\right]^{-1}\mathbf{K}_{N_R}^{-1}, \quad (24)$$

where $\left[\mathbf{I}_N + j\omega\mathbf{K}^{-1}(\mathbf{C} + j\omega\mathbf{M})\right]^{-1}$ can be expanded as follows:

$$\left[\mathbf{I}_N + j\omega\mathbf{K}^{-1}(\mathbf{C} + j\omega\mathbf{M})\right]^{-1} = \sum_{k=0}^{\infty} (-j\omega)^k \Gamma_k. \quad (25)$$

Combining (24) and (25), we get

$$\mathbf{H}(\omega) = \sum_{k=0}^{\infty} (j\omega)^k \Gamma_k. \quad (26)$$

It should be highlighted that Γ_k may be obtained specifically by the iterative approach, and only needs to be calculated once at different frequencies due to the frequency independence.

Combining (23) and (26), we provide the more broader connections between the eigensolutions and system matrices for $k = 1, 2, \ldots, \infty$, as follows:

$$-\boldsymbol{\Phi}\boldsymbol{\Theta}^{-1}\boldsymbol{\Lambda}^{-k-1}\boldsymbol{\Phi}^{\mathrm{T}} = \Gamma_k. \quad (27)$$

Hence, a novel mode superposition method called the hybrid expansion method (HEM) for calculating the displacement response can be derived. Assuming that the h term in power-series is retained for meeting appropriate precision criteria, the estimated displacement vector is shown as follows:

$$\mathbf{X}(\omega) = \sum_{i=1}^{L} \frac{\phi_i \mathbf{F}(\omega)\phi_i^{\mathrm{T}}}{\mathbf{a}_i(j\omega - \lambda_i)}$$
$$+ \sum_{r=1}^{h} (j\omega)^{r-1}\left[\Gamma_{r-1}\mathbf{F}(\omega) + \sum_{i=1}^{L} \frac{\phi_i\mathbf{F}(\omega)\phi_i^{\mathrm{T}}}{\mathbf{a}_i\lambda_i^{\mathrm{T}}}\right]. \quad (28)$$

4. Topology Optimization Model

4.1. Problem Statement.
The motive of the research is to seek for the design layouts of a given amount of damping material to minimize the vibration amplitude at the specified locations. The steady displacement response is obtained by

$$A_j = \sqrt{\left(Y_j^{\mathrm{R}}\right)^2 + \left(Y_j^{\mathrm{I}}\right)^2}, \quad (j = 1, 2, \ldots, N), \quad (29)$$

where Y_j^{R} and Y_j^{I} ($j = 1, 2, \ldots, N$) are the real and imaginary parts of the complex amplitude Y_j, respectively.

The mathematical model is established as follows:

$$\min_{\rho} f = \sum_{j=1}^{m} A_j^2,$$
$$\text{s.t.} \left(-\omega^2\mathbf{M}_{N_G} + i\omega\mathbf{C}_{N_G} + \mathbf{K}_{N_G}\right)\mathbf{Y} = \mathbf{F}_{N_G},$$
$$\sum_{e=1}^{N_e} \rho_e V_e - f_v \sum_{e=1}^{N_e} V_e^0 \leq 0, \quad (30)$$
$$0 < \rho_{\min} \leq \rho_e \leq 1, \quad (e = 1, 2, \ldots, N_e),$$

where ρ_e are the pseudodensity variables, N_e denotes the total number of desirable elements, and m is the number of specified DOFs. The volume fraction is represented by the symbol f_v. $\rho_{\min}$ is the lower bound of the design variables to prevent the system matrices from becoming singular, in this case $\rho_{\min} = 0.001$.

In the framework of the polynomial interpolation scheme (PIS), the elemental mass matrices $\mathbf{m}_v^e$ and $\mathbf{m}_c^e$ and stiffness matrices $\mathbf{k}_v^e$, $\mathbf{k}_c^e$, and $\mathbf{k}_{sv}^e$ are expressed by

$$\mathbf{m}_v^e = \rho_e\mathbf{m}_v^{e0},$$
$$\mathbf{k}_v^e = \frac{15\rho_e^5 + \rho_e}{16}\mathbf{k}_v^{e0},$$
$$\mathbf{k}_{sv}^e = \frac{15\rho_e^5 + \rho_e}{16}\mathbf{k}_{sv}^{e0}, \quad (31)$$
$$\mathbf{m}_c^e = \rho_e\mathbf{m}_c^{e0},$$
$$\mathbf{k}_c^e = \frac{15\rho_e^5 + \rho_e}{16}\mathbf{k}_c^{e0},$$

where $\mathbf{m}_v^{e0}$ and $\mathbf{m}_c^{e0}$ and $\mathbf{k}_v^{e0}$, $\mathbf{k}_c^{e0}$, and $\mathbf{k}_{sv}^{e0}$ are the mass matrices and stiffness matrices when mass density is equal to 1.

4.2. Sensitivity Analysis.
To perform optimization, the globally convergent method of moving asymptotes (GCMMA) is adopted to obtain the optimized solution. The AVM is preferred compared to the direct method for topology optimization problems involved in this study

The sensitivity of objective function in (30) is given by

$$\sum_{j=1}^{m} \frac{\partial A_j^2}{\partial\rho_e} = \sum_{j=1}^{m} 2\left(\mathrm{Re}(Y_j)\frac{\partial\mathrm{Re}(Y_j)}{\partial\rho_e} + \mathrm{Im}(Y_j)\frac{\partial\mathrm{Im}(Y_j)}{\partial\rho_e}\right), \quad (32)$$

where $\partial Y_j/\partial\rho_e$ can be derived as follows:

$$\frac{\partial Y_j}{\partial\rho_e} = \frac{\partial\left(\mathbf{L}^{\mathrm{T}}\mathbf{Y}\right)}{\partial\rho_e} = \mathbf{L}^{\mathrm{T}}\frac{\partial\mathbf{Y}}{\partial\rho_e}, \quad (33)$$

where $\mathbf{L}$ is so-called the column vector with concerned DOF j being 1.

Take the derivative of both sides of (30) with respect to the design variables as

$$\frac{\partial\mathbf{K}_d}{\partial\rho_e}\mathbf{Y} + \mathbf{K}_d\frac{\partial\mathbf{Y}}{\partial\rho_e} = 0. \quad (34)$$

Substituting (34) into (33) and taking into account the symmetry of $\mathbf{K}_d$, one obtains

$$\frac{\partial Y_j}{\partial\rho_e} = \mathbf{L}^{\mathrm{T}}\frac{\partial\mathbf{Y}}{\partial\rho_e} = -\mathbf{L}^{\mathrm{T}}\mathbf{K}_d^{-1}\frac{\partial\mathbf{K}_d}{\partial\rho_e}\mathbf{Y} = -\boldsymbol{\lambda}^{\mathrm{T}}\frac{\partial\mathbf{K}_d}{\partial\rho_e}\mathbf{Y}, \quad (35)$$

where $\boldsymbol{\lambda}$ can be calculated by following equation:

$$\mathbf{K}_d\boldsymbol{\lambda} = \mathbf{L}. \quad (36)$$

Almost no additional computation is required because of the same FRF whether the excitation load is **F** or **L**.

Once the **λ** is obtained, then the first-order sensitivity of the displacement response can be calculated as follows:

$$\frac{\partial Y_j}{\partial \rho_e} = -\boldsymbol{\lambda}^{\mathrm{T}}\left(-\omega^2 \frac{\partial \mathbf{M}_{N_G}}{\partial \rho_e} + j\omega \frac{\partial \mathbf{C}_{N_G}}{\partial \rho_e} + \frac{\partial \mathbf{K}_{N_G}}{\partial \rho_e}\right)\mathbf{Y}. \qquad (37)$$

The first-order sensitivity of the augmented global matrix, namely, the mass, stiffness and damping matrices in (37), can be obtained by the chain rule through interpolation relations in (31) at the element level. Then, remaining derivatives of the corresponding sensitivity are removed.

4.3. Topology Optimization Process. The sensitivity filtering scheme based on the image [33] is applied to avoid checkerboard and mesh dependence. The filter modifies the design sensitivity of a specific element based on a weighted average of the element sensitivities in a fixed neighborhood, which is purely heuristic but produces results very similar to local gradient-constrained results, requiring little extra CPU time. The GCMMA algorithm [34] is used to find the optimal solution. All cases are performed in the commercial software MATLAB R2018a. The optimization process will stop until the absolute error of the design objectives satisfies $\|(f_{\mathrm{new}} - f_{\mathrm{old}})/f_{\mathrm{old}}\| < 0.0005$. Figure 3 presents the flow diagram of the optimization process.

5. Numerical Examples

This section presents two typical numerical examples with different boundary conditions. One is a cantilever plate clamped at the left side, as shown in Figure 4(a). An external force $f(t) = Fe^{i\omega t}$ is applied at the midpoint of the right side, with $F = 10^5$N and $\omega = 2\pi f_{\mathrm{p}}$. The other is the structure clamped by four sides shown in Figure 4(b), and the same external force is applied at the center of the plate. For viscoelastic composite structures, the material 1 called 242F01, manufactured by 3M, is employed as the damping layer, which exhibits frequency and temperature dependence. Table 1 presents the material properties for the viscoelastic plate. The modulus of 242F01 is characterized by the GHM model. The parameters at $10°C$ and $25°C$ are obtained through the dynamic mechanical analysis (DMA) and least square method and are given in Table 2. For comparison, material 2 is an artificial material, characterized by the complex constant model, whose properties are obtained by averaging the modulus of 242F01 in the frequency domain. This section first investigates the validity of response and sensitivity analysis, then verifies the validity of introducing the dynamic reduction method into topology optimization. Next, the performance of the proposed optimization methods are compared in detail. Finally, the impact of the viscoelastic material's frequency- and temperature-dependent properties on optimal layouts is emphatically analyzed. Furthermore, the influence of layer thicknesses and volume fractions on optimal layouts of damping material is further discussed. In order to

quantitatively characterize the correlation between different optimal layouts, the similarity index is defined as follows:

$$SI = \frac{S_{\mathrm{same}}}{S_{\mathrm{total}}}, \qquad (38)$$

where S_{same} is the overlapped area of damping layer between the different optimal layouts and S_{total} is the total area of damping layer. However, since the relative density is not the absolute 0-1 distribution, the calculation accuracy of the overlap area between different optimized configurations is the possible potential limitation.

Although some researchers have shown that solid elements have higher computational accuracy, they then have much lower computational efficiency. Therefore, comparisons in the accuracy and efficiency of the calculated results between the proposed model and common commercial software ANSYS are conducted. For the numerical model in ANSYS, the structure is discrete into 40×40 three-dimensional continuous solid elements. The results are in line with expectations. Under the premise of less than 3.42% error of calculation accuracy, the CPU time of the proposed model is significantly reduced by 74.8% compared with common commercial software, ANSYS. The excellent performance of the proposed model in terms of precision and efficiency is fully demonstrated.

In order to verify the effectiveness of the proposed strategy combining modal polycondensation and hybrid expansion for solving frequency- and temperature-dependent optimization design problems, the comparison of optimal design, as shown in Figure 4(a) between full-order and reduced-order models is carried out in this section. The volume fraction of the damping material is set at 50%, and the initial layout is uniform distribution with a mass density of 0.5. An excitation frequency of $f_{\mathrm{p}} = 100$Hz is considered. Figure 5 presents the iterative process of the optimal layouts and objective functions for the full-order and reduced-order models in the topology optimization. The performance comparison details during the optimization process are listed in Table 3.

Obviously, it can be observed from the iteration histories shown in Figure 5 that all design objectives decrease from $0.073\mathrm{m}^2$ to $0.011\mathrm{m}^2$ and converge to the optimal value. The reduced-order and full-order models are highly consistent in the initial and converged objective values, especially the similarity index of the two, which is as high as 99%, and nearly identical optimal configurations are obtained. Furthermore, in terms of computing time, the full-order model takes 976.9 s, while the reduced-order model only requires 213.3 s, and the acceleration ratio reaches 78.17%. It proved that the proposed strategy is feasible, which significantly improves optimization efficiency and also provides potential and possibility for topology optimization of large-scale nonproportional damping structures.

5.1. A Cantilever Plate. This section focuses on the structure shown in Figure 4(a) to investigate the influence of the response-solving methods and frequency- and temperature-dependent viscoelastic materials on the optimal configuration and vibration suppression of the CLD plate.
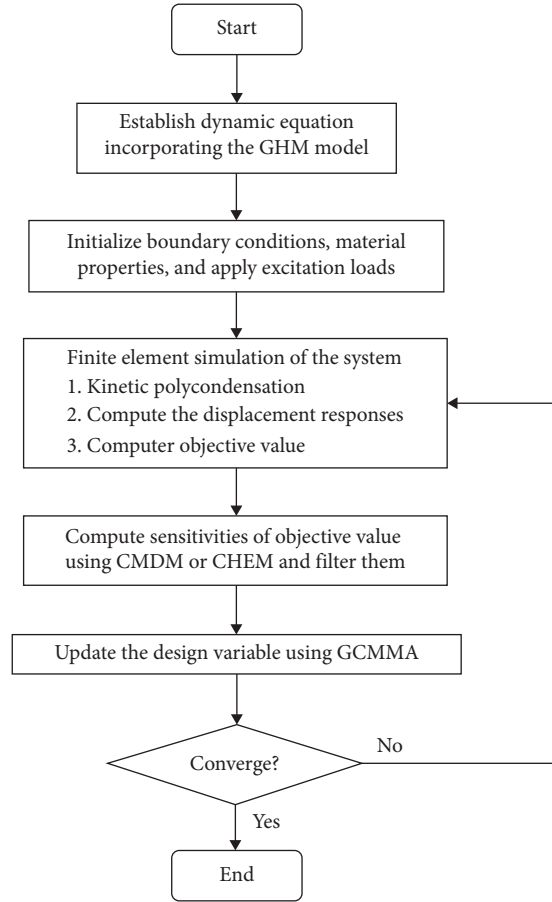
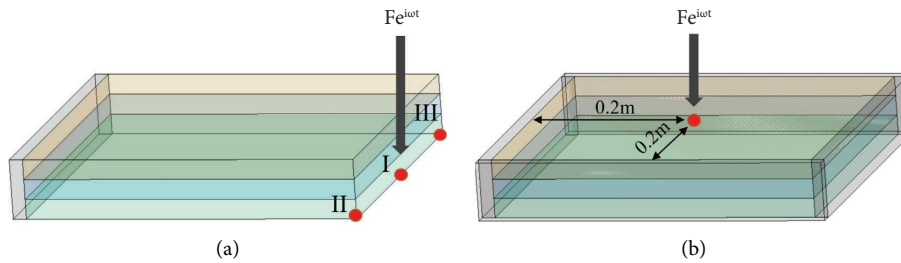FIGURE 3: The flowchart of the optimization process.

| (a) | (b) |

FIGURE 4: The viscoelastic plate with different boundary conditions. (a) A cantilever plate. (b) A plate clamped by sides.

TABLE 1: Materials and geometric parameters of the CLD plate.

CLD structure	Thickness (mm)	Density (kg/m^3)	Young's modulus (GPa)	Poisson ratio
Base layer	1.2	7900	211	0.3
Damping layer	0.6	1140	$G(\omega)$	0.4
Constrained layer	0.6	2780	71	0.3
Dimensions			$0.4 \times 0.4 \,(\text{m}^2)$	

5.1.1. Response-Solving Methods. Here, the design domain is discretized into a total of 400 elements as shown in Figure 6. Figures 7(a) and 7(b) present the comparisons of the displacement amplitudes (points I and II) and the sensitivities (elements numbered 30, 210, and 370, denoted by blue elements in Figure 6) obtained with different methods. The results calculated by the direct frequency response method (DRFM) and finite difference method (FDM) are regarded as the exact results of the displacement response and sensitivity, respectively. The detailed error comparisons are

TABLE 2: GHM parameters at different temperatures of the 242F01.

Temperature	Parameters	Mini-oscillator terms		
		First order	Second order	Third order
$T = 10°C$	G^∞		0.0091276	
	$\hat{\alpha}_k$	573.76	47889	1609.7
	$\hat{\zeta}_k$	7893.7	197.56	2304.1
	$\hat{\omega}_k$	1035800	1725500	3114500
$T = 25°C$	G^∞		0.0047868	
	$\hat{\alpha}_k$	991.58	74588	1209.9
	$\hat{\zeta}_k$	33329	62.683	5572.8
	$\hat{\omega}_k$	2107100	2534800	2544100
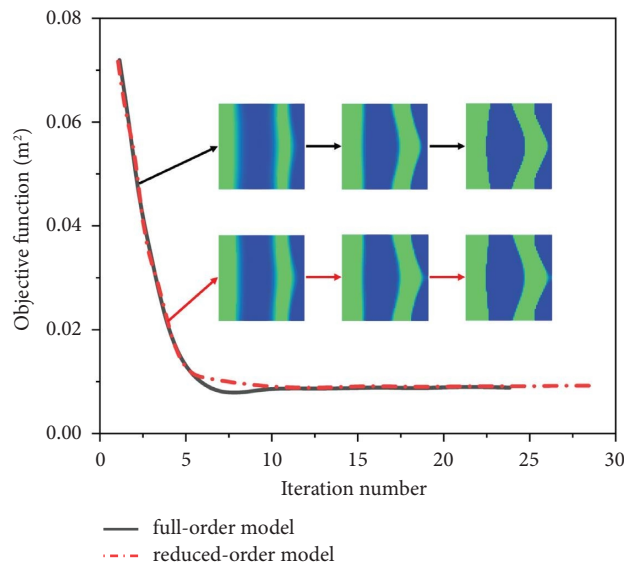
FIGURE 5: Iterative process of full-order and reduced-order models.

TABLE 3: Performance comparison of topology optimization.

Optimization model	Initial value	Converged value	CPU time (s)	SI
Full-order	0.073	0.011	976.9	0.99
Reduce-order	0.073	0.011	213.3	

depicted in the form of the line chart, as shown in Figure 7(c). For the sake of the narrative, the combination of MDM and HEM with the dynamic reduction method is, respectively, abbreviated CMDM ($q = 30$, 50, namely, i, ii) and CHEM ($h = 2$, 3, namely, iii, iv). As expected, the CHEM results agree well with the exact results, especially when h is equal to 3. The errors of the vibration amplitudes A_I and A_{II} are only 1.01% and 0.78%, respectively, and the sensitivity differences of the three specified elements are less than 2%, about 0.92%, 1.02%, and 1.33%, respectively.

However, there is a significant gap in the performance of calculation accuracy for the traditional method (i.e., CMDM). Although the vibration amplitudes retain a reasonable accuracy of around 20% when the limited low-order modes are involved (e.g., $q = 30$), the sensitivity analysis error has increased dramatically to over 30%. A negative phenomenon worthy of attention is that when the number of low-order modes involved reaches 50, however the accuracy

of sensitivity analysis cannot be guaranteed, indicating that excessive increase in the number of low-order modes is not a cost-effective measure worth popularizing.

Table 4 lists the computing times of the different methods for responses and sensitivities analysis. It can be observed that CHEM, both for response and sensitivity analysis, shows remarkable advantages in computational efficiency. As previously stated, this is because of the fact that the proposed method can achieve expected accuracy as long as it contains all modes with eigenfrequencies within the excitation frequency range, without worrying about the trade-off between computational accuracy and efficiency.

For the cantilever plate structure shown in Figure 4(a), through modal analysis, Figure 8 presents the mode shapes, and the first 6 natural frequencies are obtained as 58 Hz, 97 Hz, 142 Hz, 195 Hz, 242 Hz, and 304 Hz, respectively. As well known, damping effects are mostly observed around each natural frequency. Therefore, the excitation frequency
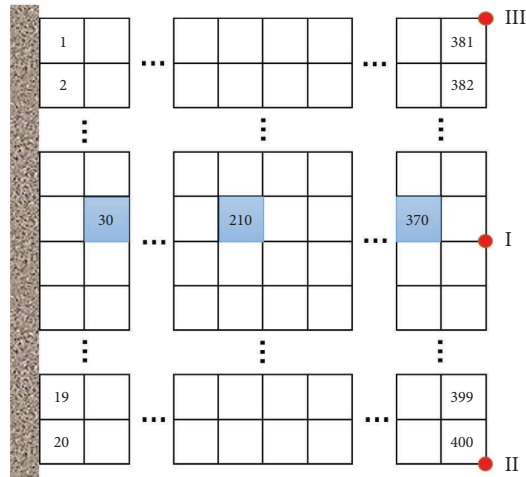
FIGURE 6: Finite element mesh and element numbers.
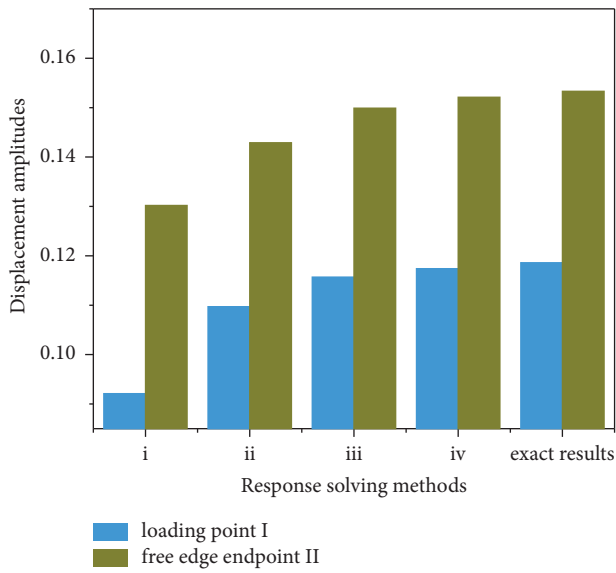
(a)
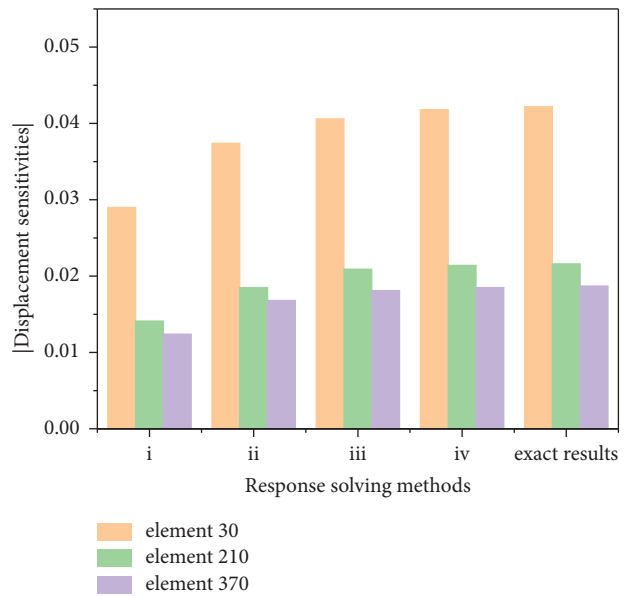
(b)

FIGURE 7: Continued.

(c)
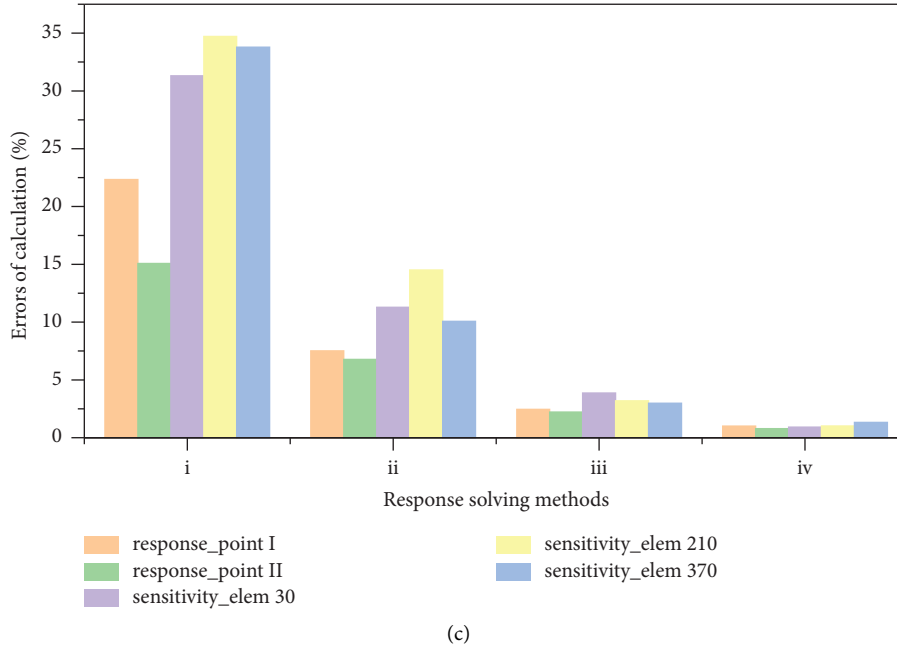
FIGURE 7: Comparison of response and sensitivity analysis for different methods. (a) Displacement amplitudes. (b) Displacement sensitivities. (c) Analysis errors.

TABLE 4: Comparison of computing time for responses and sensitivities.

	Comparison	DFRM	FDM	CMDM		CHEM	
				$q = 30$	$q = 50$	$h = 2$	$h = 3$
Time (s)	Responses	6.791		3.121	4.966	1.795	1.874
	Sensitivities		256.751	1.852	2.721	0.811	0.833

points are selected around the natural frequency, whose values are 100 Hz, 200 Hz, and 300 Hz, respectively. Table 5 depicts the optimal layouts and iteration curves of topology optimization at three different frequencies (i.e., f_p = 100 Hz, 200 Hz, and 300 Hz) and also lists the optimization details. The blue and green color in optimal material configurations represent the area covered by the damping layer and without the damping layer, respectively. On the one hand, the damping materials obtained by topological optimization are mainly distributed in the region with larger modal strain energy determined by adjacent mode shapes. On the other hand, the distribution of damping materials tends to be complicated and decentralized with the increase of the excitation frequency. The reason is that higher excitation frequencies are prone to excite higher-order modes with more localized characteristics. This can also be confirmed by the obtained vibration shape from the lower-order to the higher-order modes, showing a consistent variation trend. It can be seen that the optimal configurations based on the two methods have a high degree of similarity, with the values of 0.79, 0.89, and 0.84, indicating that both methods can obtain reasonable configurations despite the difference in calculation accuracy.

However, there are also significant differences in convergence and clarity. This simulation results show that CHEM works well while CMDM converges poorly when

large-scale problems are considered, as evidenced by the fluctuation of the initial stage and the oscillation of the later stage in the iterative curves. It can be concluded that high-precision response and sensitivity analysis methods are more conducive to improving the convergence of topology optimization and obtaining the expected results. The reasons come from the two aspects. On the one hand, CMDM, as an approximate method, inevitably introduces truncation errors especially for sensitivity analysis, which may cause deviations or even errors in the optimization direction. On the other hand, large errors will be generated away from the resonant frequency, and the essence of dynamic response optimization is to drive the resonant frequency away from the excitation frequency to reduce the vibration level, which further reduces the accuracy of response and sensitivity analysis. This may explain why low-precision analysis methods are by far not entirely satisfactory for large-scale optimization design problems.

According to the details in Table 5, CHEM can reduce 70.53%, 65.63%, and 65.69% CPU time for cases of different frequencies, respectively. The performance on computational efficiency is due to the fact that the CHEM-based method only needs to consider the low-order modes within the excitation frequency rather than enough low-order modes, the order of which can be adaptively determined according to the varied structural eigenfrequencies in each
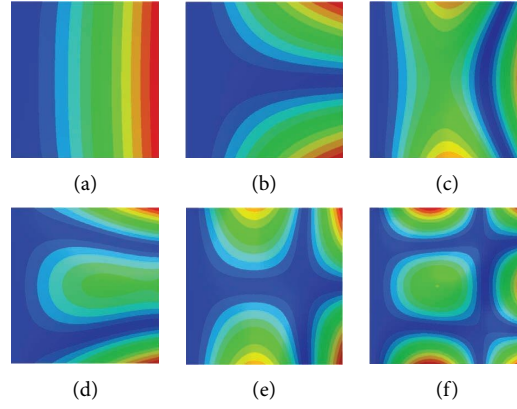
FIGURE 8: The mode shapes of the cantilever plate. (a) 1st mode. (b) 2nd mode. (c) 3rd mode. (d) 4th mode. (e) 5th mode. (f) 6th mode.

TABLE 5: The topology optimization results of the cantilever plate based on different solution methods.

Frequency	CMDM	CHEM	Iterative curve
100 Hz			
CPU time	723.7 s	213.3 s	SI: 0.79
Objective value	$0.065 \longrightarrow 0.014 \, \text{m}^2$	$0.073 \longrightarrow 0.011 \, \text{m}^2$	
200 Hz			
CPU time	1113.9 s	382.8 s	SI: 0.89
Objective value	$0.133 \longrightarrow 0.024 \, \text{m}^2$	$0.149 \longrightarrow 0.019 \, \text{m}^2$	
300 Hz			
CPU time	1662.9 s	570.4 s	SI: 0.84
Objective value	$0.182 \longrightarrow 0.026 \, \text{m}^2$	$0.214 \longrightarrow 0.021 \, \text{m}^2$	

iteration, which greatly reduces the surge of computational time caused by complex modal analysis and multiple iterations.

5.1.2. Frequency- and Temperature-Dependent Properties.

The frequency-dependent properties of viscoelastic material at 10°C and 25°C are considered. To design an artificial modulus at room temperature as the comparison group, the averaged real and imaginary part of modulus at 25°C are obtained, given by $G_v = 8.4(1 + 1.72j)$MPa. Figure 9 presents the frequency-dependent and averaged shear moduli of 242F01 for 10°C and 25°C. Obviously, the stiffness and damping performance of 242F01 exhibit significant changes with frequencies and temperatures varying.

The optimal layouts and iteration curves induced by the complex constant model and GHM model are presented in Table 6. The quantitative details are also listed. Since the cantilever plate structure has not changed, the excitation frequencies are still selected as 100 Hz, 200 Hz, and 300 Hz. In general, the optimal layouts obtained all exhibit remarkable convergence. However, there are significant differences among the design layouts of damping materials. The reason comes from the fact that the frequency and temperature dependence of viscoelastic materials can influence the stiffness distribution and damping behavior of CLD structures. Generally speaking, the similarity index of SI-II in the corresponding group is the highest, which is because the complex constant model adopts the average value of the complex modulus of the GHM model at $T = 25$°C. However,
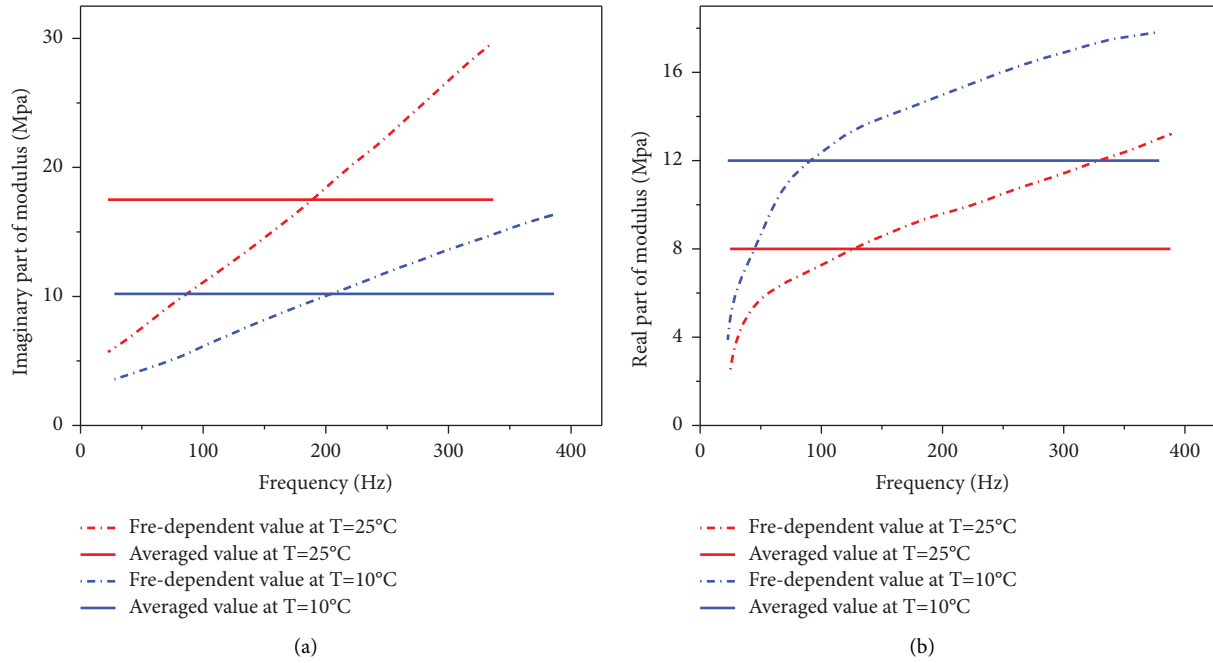
FIGURE 9: Frequency-dependent and averaged shear moduli for 242F01. (a) Real part. (b) Imaginary part.

due to the discrepancy between the averaged and actual moduli at different frequencies, the similarity of the SI-II group at $f_p = 300$Hz was 0.702, which was significantly lower than that of 0.862 at $f_p = 200$Hz. Furthermore, most of the similarities in the SI-I and SI–III groups were at a low level, with two being lower than 0.5 (0.429, 0.441) and two being in the range of 0.5–0.7 (0.579, 0.591, 0.687). This phenomenon is clearly caused by changes in temperature and frequency caused by the viscoelastic material properties of the great change. In addition, it can be observed that the similarity indices corresponding to $f_p = 300$Hz are significantly lower than that of $f_p = 200$Hz. This attributes to significant changes in the optimized configuration at higher frequencies due to the involvement of more local modes, even if temperature makes a limited difference.

5.2. A Plate Clamped by Four Sides. To further validate the accuracy and efficiency of the proposed CHEM-based approach and to compare the effect of frequency- and temperature-dependent properties of damping material on optimal layouts and vibration suppression, the CLD structure is considered under another boundary condition, as shown in Figure 4(b), which is clamped by four sides, representing more "rigid" boundary conditions. The optimization objectives are to minimize the sum of squares of vibration amplitudes at specific points of concern as indicated by the red dots in Figure 5.
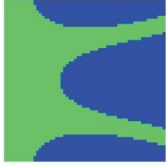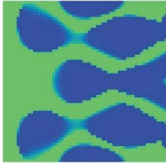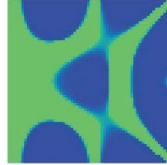
5.2.1. Response-Solving Methods. For the plate structure clamped by four sides shown in Figure 4(b), through modal analysis, Figure 10 gives the mode shapes, and the first 6 natural frequencies are obtained as 128 Hz, 197 Hz, 289 Hz, 392 Hz, 428 Hz, and 511 Hz, respectively. Therefore, the

selection strategy of frequency points is based on the natural frequencies, where the values are 200 Hz, 400 Hz, and 500 Hz, respectively.

Table 7 depicts the optimal layouts and iteration curves and also presents the performance results of topology optimization. A similar phenomenon can be observed that the optimization results obtained by the two methods present obvious differences while maintaining similarities. In general, the damping materials are concentrated in the region of the larger modal strain energy in the corresponding modes, and the distribution tends to be local and dispersed with the increase in excitation frequency. The similarity indices between the optimal layouts obtained are relatively high, with values of 0.92, 0.83, and 0.81, respectively. The CHEM-based optimization method can obtain clear optimal layouts due to its high accuracy, and the strong convergence is also demonstrated by iterative curves. However, the detailed characteristics of optimization configuration based on CMDM, with obvious oscillation and fluctuations existing in curves, presented unclear and ambiguous results, and a complete 0-1 distribution cannot be formed, especially the optimal layout corresponding to $f_p = 400$Hz. The reason is also the cumulative error in response and sensitivity analysis due to modal truncation, particularly for large-scale structures. Equally important, topology optimization based on CHEM also has clear advantages in computing efficiency, which can be reduced by 66.65%, 70.49%, and 69.73% CPU time when compared with CMDM.

5.2.2. Frequency- and Temperature-Dependent Properties. The optimal layouts and quantitative similarity indices induced by complex constant modulus and frequency-dependent modulus are presented in Table 8. The specific temperature points are chosen as 10°C and 25°C, and the

TABLE 6: The topology optimization results of the cantilever plate based on different damping models.

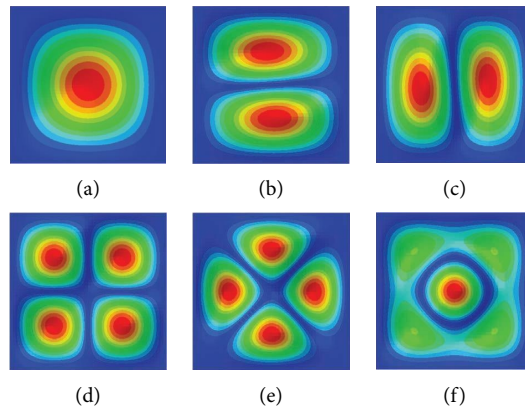| Frequency	(i) 10°C	(ii) 25°C	(iii) Complex constant
100 Hz	SI-I(i, iii): 0.429	SI-II(ii, iii): 0.899	SI-III(i, ii): 0.441
200 Hz	SI-I(i, iii): 0.687	SI-II(ii, iii): 0.862	SI-III(i, ii): 0.717
300 Hz	SI-I(i, iii): 0.579	SI-II(ii, iii): 0.702	SI-III(i, ii): 0.591

FIGURE 10: The mode shapes of the plate clamped by four sides. (a) 1st mode. (b) 2nd mode. (c) 3rd mode. (d) 4th mode. (e) 5th mode. (f) 6th mode.

TABLE 7: The topology optimization results of the plate clamped by four sides based on different solution methods.
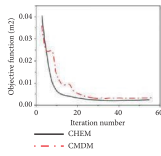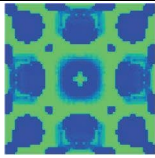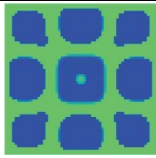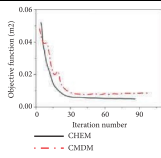
Frequency	CMDM	CHEM	Iterative curve
200 Hz			
CPU time	1225.8 s	408.8 s	SI: 0.89
Objective value	$0.036 \longrightarrow 0.005 \, \text{m}^2$	$0.041 \longrightarrow 0.004 \, \text{m}^2$	
400 Hz			
CPU time	2244.3 s	662.2 s	SI: 0.81
Objective value	$0.048 \longrightarrow 0.009 \, \text{m}^2$	$0.052 \longrightarrow 0.007 \, \text{m}^2$	

TABLE 7: Continued.
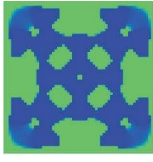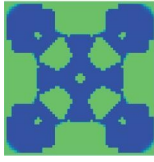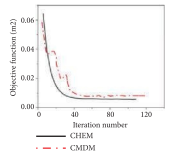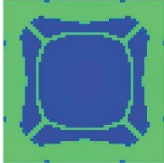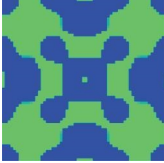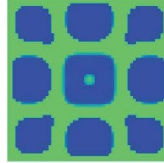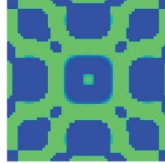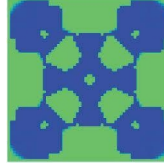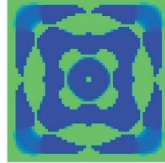
Frequency	CMDM	CHEM	Iterative curve
500 Hz			
CPU time	2783.0 s	842.4 s	SI: 0.86
Objective value	0.059 ⟶ 0.013 m^2	0.065 ⟶ 0.011 m^2	

TABLE 8: The topology optimization results of the plate clamped by four sides based on different damping models.

Frequency	(i) 10°C	(ii) 25°C	(iii) Complex constant
200 Hz	SI-I(i, iii): 0.617	SI-II(ii, iii): 0.831	SI–III(i, ii): 0.539
400 Hz	SI-I(i, iii): 0.642	SI-II(ii, iii): 0.901	SI–III(i, ii): 0.601
500 Hz	SI-I(i, iii): 0.437	SI-II(ii, iii): 0.611	SI–III(i, ii): 0.411

excitation frequency remain the same as in the previous section, i.e., 200 Hz, 400 Hz, and 500 Hz.

The optimal layouts of CLD structures differ significantly, which can be attributed to the great changes in mechanical properties of viscoelastic materials at different temperatures. Although taking the average value to approximate the frequency-dependent properties of damping material at room temperature obtains a relatively properly optimized configuration, differences that cannot be ignored still exist objectively. For complex structures and conditions, the discrepancies in the optimized configuration may be magnified and result in unexpected influences. One also notes that at higher frequencies, such as 500 Hz, the similarity indices for different optimized configurations are significantly lower than those at lower frequencies. This is because higher frequency excites higher-order eigenmodes with more local characteristics, which are more sensitive to the stiffness and damping performance of viscoelastic materials, leading to a more differentiated optimal configuration. It is reasonable to infer that the similarity of the optimized configuration will further decrease with increasing temperature differences, even obtaining uncontrollable erroneous results.

5.2.3. Excitation of the Frequency Bands. This section further discusses the optimal configuration of damping materials under frequency-band excitation. The temperature is 10°C and 25°C, respectively, and the scheme of the excitation frequency band corresponds to the natural frequency of the structure, which is set to [0 − 200]Hz, [0 − 400]Hz, and [0 − 500]Hz, respectively. Table 9 shows the optimal configuration of the damping material excited by the frequency band at different temperatures. Firstly, the distribution of damping materials at different temperatures is quite different, and the similarity indices are only 0.79, 0.74, and 0.66, respectively. Secondly, the configuration of damping materials obtained by frequency band and discrete excitation is inconsistent at specific temperature points, which is also the result of the synergy of discrete frequency points in the frequency band.

TABLE 9: The topology optimization results under the frequency band at different temperatures.
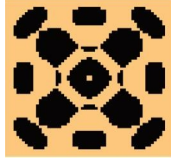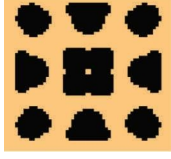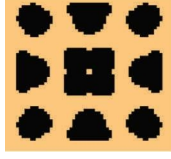
Frequency	(i) [0 − 200]Hz	(ii) [0 − 400]Hz	(iii) [0 − 500]Hz
10°C			
25°C			

TABLE 10: Different thicknesses of damping and constrained layers.

Group number	1	2	3	4	5	6
Constrained layer (mm)	0.78	0.72	0.66	0.6	0.54	0.48
Damping layer (mm)	0.15	0.3	0.45	0.6	0.75	0.9
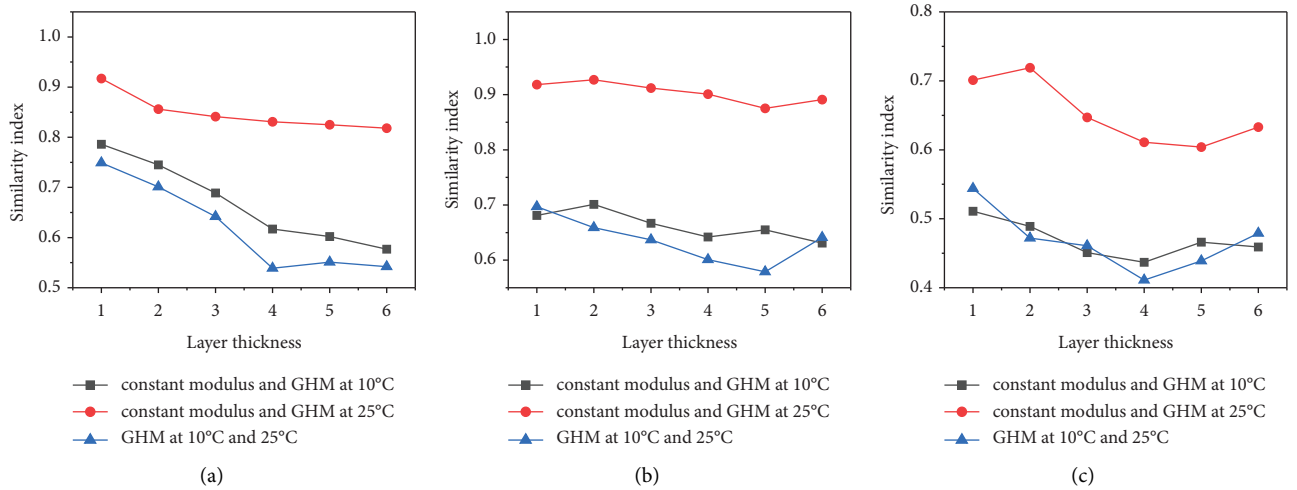
FIGURE 11: Variation of similarity indices for optimal configuration with layer thicknesses. (a) $f_p = 100$ Hz. (b) $f_p = 200$ Hz. (c) $f_p = 300$ Hz.

5.2.4. Discussion of Layer Thicknesses and Volume Fractions.
Layer thickness and volume fraction have been given a lot of attention as two main parameters affecting the configuration of damping materials. At different temperatures, without changing the mass of the CLD material, i.e., the total mass of the damping layer and the constrained layer is constant, the similarity indices between the optimal layout induced by averaged and frequency-dependent shear moduli for different thicknesses of the layer are discussed in detail.

Table 10 lists the six groups with different thicknesses of damping and constrained layers. Figure 11 presents the similarity variation trend of optimal configurations of averaged modulus as well as frequency- and temperature-dependent moduli obtained by changing the thickness of the constrained layer and damping layer. It can be observed that the optimal layouts obtained by the GHM model and averaged complex modulus at 25°C has a high similarity,

while the similarities of other cases are at a low level, and the similarity gradually decreases with the increase in excitation frequency. In addition, it is concluded that the similarity of the optimal configuration at different temperatures is negatively correlated with the thickness of the damping layer at all three excitation frequencies. However, the above studies are qualitative analyses rather than quantitative description. Moreover, the conclusions taken from the results are restricted to the small set of thickness pairs herein considered. In fact, as Sher and Moreira [35] point out, the effect of the thickness of both layers, constraining and damping layers, is quite more complex and does not follow a monotonic behavior. Therefore, future work will be devoted to further exploring the effects of the thickness of each layer.

Fixing the thickness of damping and constrained layers, we consider the influence of the different volume fractions, with $f_v = 0.3, 0.4, 0.5, 0.6, 0.7$, and 0.8, respectively. Figure 12
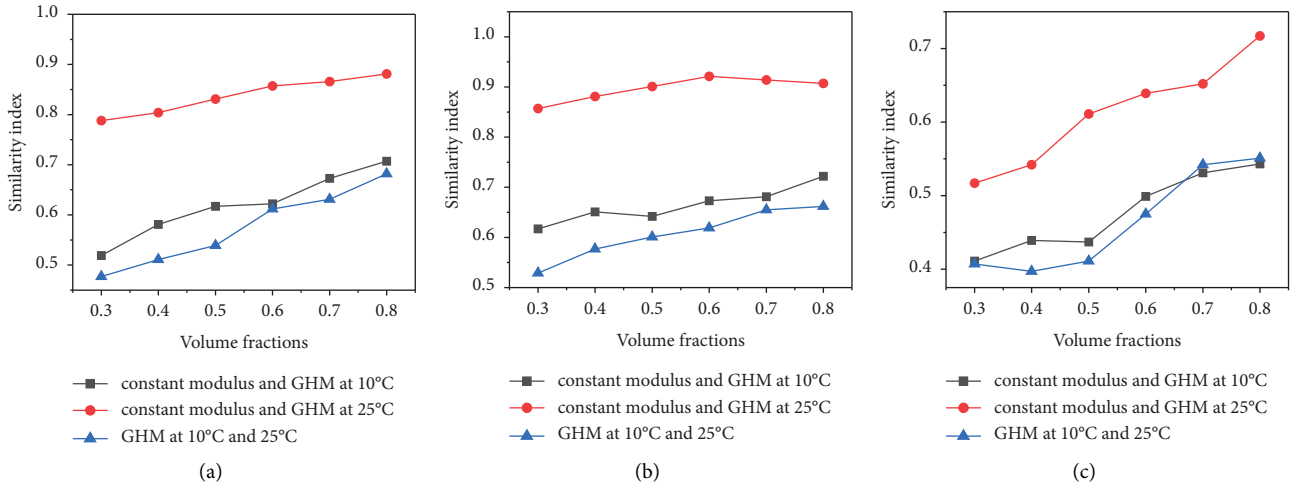
FIGURE 12: Similarity indices between optimized layouts with varied volume fractions. (a) $f_p = 100$ Hz. (b) $f_p = 200$ Hz. (c) $f_p = 300$ Hz.

illustrates the comparison results. Obviously, higher excitation frequency corresponds to lower similarities. Furthermore, the similarity indices at different frequencies show a roughly close increasing trend with the increase in volume fraction of the damping material. As a result, it is particularly necessary to consider the frequency and temperature dependence of damping materials for topology optimization of viscoelastic structures under the requirement of lower volume fractions.

6. Conclusions

This paper investigates topology optimization of CLD structures comprising frequency- and temperature-dependent viscoelastic material under harmonic excitations. The structure is characterized by a nonproportional damping model. A novel approach combining hybrid expansion and dynamic reduction methods, which can deal with nonproportional damping, is proposed and developed to solve the topology optimization problem. The objective functions are chosen as the sum of the squared vibration amplitudes of the concerned points. The sensitivity analysis is implemented by using the adjoint variable method. The similarity index is suggested to quantitatively distinguish the different optimal layouts of damping materials. The conclusions can be drawn as follows:

(1) The involved optimization design problem is essentially a highly nonconvex issue with multiple local optima. Two typical examples demonstrate that the proposed approach not only obtains clear and convergent optimal layouts of damping material but also significantly reduces computational time. The massive improvement in efficiency becomes more meaningful for composite structures with larger DOFs.

(2) The frequency and temperature dependence of viscoelastic materials remarkably affect the optimized configuration of CLD structures. The reason is that the change in temperature and frequency will cause

great fluctuations in the mechanical properties and energy dissipation of the viscoelastic material, which mainly decides the dynamic optimization results.

(3) In the future research, taking into account the fluctuation of material properties caused by the frequency and temperature, it is quite promising to extend the proposed approach to other types of viscoelastic structures rather than just CLD structures and to carry out more refined topology optimization design when subjected to broadband random excitations or even wide-range temperatures.

Data Availability

The data used to support the findings of this study are available from the corresponding author upon request.

Conflicts of Interest

The authors declare that they have no conflicts of interest.

Authors' Contributions

Fan Wu is contributed equally.

Acknowledgments

References

[1] A. Sofiyev and J. L. Whitton, "About an approach to the determination of the critical time of viscoelastic functionally graded cylindrical shells," *Composites Part B: Engineering*, vol. 156, pp. 156–165, 2019.

[2] V. C. Haciyev, A. H. Sofiyev, and N. Kuruoglu, "On the free vibration of 566 orthotropic and inhomogeneous with spatial coordinates plates resting on 7 the inhomogeneous

viscoelastic foundation," *Mechanics of Advanced Materials and Structures*, vol. 26, pp. 1–12, 2018.

[3] X. T. Cao, Z. Y. Zhang, and H. X. Hua, "Free vibration of circular cylindrical shell with constrained layer damping," *Applied Mathematics and Mechanics*, vol. 32, no. 4, pp. 495–506, 2011.

[4] K. Akoussan, H. Boudaoud, E. M. Daya, Y. Koutsawa, and E. Carrera, "Numerical method for nonlinear complex eigenvalues problems depending on two parameters: application to three-layered viscoelastic composite structures," *Mechanics of Advanced Materials and Structures*, vol. 25, no. 15-16, pp. 1361–1373, 2017.

[5] H. Li, T. F. Wu, Z. J. Gao et al., "An iterative method for identification of temperature and amplitude dependent material parameters of fiber-reinforced polymer composites," *International Journal of Mechanical Sciences*, vol. 184, Article ID 105818, 2020.

[6] M. A. Trindade, A. Benjeddou, and R. Ohayon, "Modeling of frequency dependent viscoelastic materials for active-passive vibration damping," *Journal of Vibration and Acoustics*, vol. 122, no. 2, pp. 169–174, 2000.

[7] H. Zheng, C. Cai, and X. M. Tan, "Optimization of partial constrained layer damping treatment for vibrational energy minimization of vibrating beams," *Computers & Structures*, vol. 82, no. 29-30, pp. 2493–2507, 2004.

[8] M. X. Wang and G. P. Chen, "Dynamics performance optimization of cylindrical shell with constrained damping layer using homogenization approach," *China Mechanical Engineering*, vol. 22, no. 8, pp. 892–897, 2011.

[9] S. Y. Kim, C. K. Mechefske, and I. Y. Kim, "Optimal damping layout in a shell structure using topology optimization," *Journal of Sound and Vibration*, vol. 332, no. 12, pp. 2873–2883, 2013.

[10] Y. Xu, W. Gao, Y. Yu et al., "Dynamic optimization of constrained layer damping structure for the headstock of machine tools with modal strain energy method," *Shock and Vibration*, vol. 2017, no. 10, Article ID 2736545, 13 pages, 2017.

[11] H. Zhang, A. Takezawa, X. H. Ding, H. H. Guo, W. Y. Ni, and X. P. Zhang, "Topology optimization of composite macrostructures comprising multi-phase viscoelastic composite microstructures for enhanced structural damping," *Composite Structures*, vol. 278, Article ID 114712, 2021.

[12] Z. Fang and L. Zheng, "Topology optimization for minimizing the resonant response of plates with constrained layer damping treatment," *Shock and Vibration*, vol. 2015, no. 2, Article ID 376854, 11 pages, 2015.

[13] W. G. Zheng, T. L. Yang, Q. B. Huang, and Z. He, "Topology optimization of pcld on plates for minimizing sound radiation at low frequency resonance," *Structural and Multidisciplinary Optimization*, vol. 53, no. 6, pp. 1231–1242, 2016.

[14] A. Takezawa, M. Daifuku, Y. Nakano, K. Nakagawa, T. Yamamoto, and M. Kitamura, "Topology optimization of damping material for reducing resonance response based on complex dynamic compliance," *Journal of Sound and Vibration*, vol. 365, no. 6, pp. 230–243, 2016.

[15] A. Delisse N, F. van Keulen, and M. Langelaar, "Efficient limitation of resonant peaks by topology optimization including modal truncation augmentation," *Structural and Multidisciplinary Optimization*, vol. 61, no. 6, pp. 2557–2575, 2020.

[16] Z. Kang, X. P. Zhang, S. G. Jiang, and G. D. Cheng, "On topology optimization of damping layer in shell structures under harmonic excitations," *Structural and Multidisciplinary Optimization*, vol. 46, no. 1, pp. 51–67, 2012.

[17] X. P. Zhang and Z. Kang, "Topology optimization of damping layers for minimizing sound radiation of shell structures," *Journal of Sound and Vibration*, vol. 332, no. 10, pp. 2500–2519, 2013.

[18] A. H. Sofiyev, "On the solution of the dynamic stability of heterogeneous orthotropic visco-elastic cylindrical shells," *Composite Structures*, vol. 206, pp. 124–130, 2018.

[19] A. H. Sofiyev, Z. Zerin, and N. Kuruoglu, "Dynamic behavior of fgm viscoelastic plates resting on elastic foundations," *Acta Mechanica*, vol. 231, no. 1, pp. 1–17, 2020.

[20] H. Li, Z. Wang, H. Lv et al., "Nonlinear vibration analysis of fiber reinforced composite cylindrical shells with partial constrained layer damping treatment," *Thin-Walled Structures*, vol. 157, no. 4, Article ID 107000, 2020.

[21] I. K. Oh, "Damping characteristics of cylindrical laminates with vis-coelastic layer considering temperature- and frequency-dependence," *Journal of Thermal Stresses*, vol. 32, no. 1-2, pp. 1–20, 2008.

[22] G. Q. Shu, W. L. Zhao, X. Y. Liang, Y. Chen, and X. X. Sun, "Vibration analysis and optimization of composite structure with constrained-layer damping treatment," *Hsi-An Chiao Tung Ta Hsueh/Journal of Xi'an Jiaotong University*, vol. 48, no. 3, pp. 108–114, 2014.

[23] M. Mokhtari, M. R. Permoon, and H. Haddadpour, "Dynamic analysis of isotropic sandwich cylindrical shell with fractional viscoelastic core using Rayleigh–ritz method," *Composite Structures*, vol. 186, pp. 165–174, 2018.

[24] W. Sun, X. Yan, and Z. Wang, "Analysis of the effects of frequency dependent characteristic on the vibration of vis-coelastic composite structure," *Journal of Mechanical Engineering*, vol. 54, no. 5, pp. 121–128, 2018.

[25] Q. Dai, Z. Qin, and F. Chu, "Parametric study of damping characteristics of rotating laminated composite cylindrical shells using haar wavelets," *Thin-Walled Structures*, vol. 161, no. 1, Article ID 107500, 2021.

[26] D. D. Zhang, Y. H. Wu, X. Lu, and L. Zheng, "Topology optimization of constrained layer damping plates with frequency- and temperature-dependent viscoelastic core via parametric level set method," *Mechanics of Advanced Materials and Structures*, vol. 29, no. 1, pp. 154–170, 2021.

[27] D. J. Mctavish and P. C. Hughes, "Modeling of linear viscoelastic space structures," *Journal of Vibration and Acoustics*, vol. 115, no. 1, pp. 103–110, 1993.

[28] D. F. Golla and P. C. Hughes, "Dynamics of viscoelastic structures—a time domain, finite element formulation," *Journal of Applied Mechanics*, vol. 52, no. 4, pp. 897–906, 1985.

[29] L. Li, Y. Hu, X. Wang, and L. Lü, "A hybrid expansion method for frequency response functions of non-proportionally damped systems," *Mechanical Systems and Signal Processing*, vol. 42, no. 1-2, pp. 31–41, 2014.

[30] Y. T. Leung, "An accurate method of dynamic condensation in structural analysis," *International Journal for Numerical Methods in Engineering*, vol. 12, no. 11, pp. 1705–1715, 1978.

[31] N. Petersmann, "Calculation of eigenvalues using substructures and dynamic condensation," *Calculation Ofgenvalues Using Substructures and Dynamic Condensation*, vol. 12, no. 11, pp. 1705–1715, 1984.

[32] Z. Q. Qu, H. X. Hua, and Z. F. Fu, "A coordinate dynamic condensation technique for finite element model," *Shock and Vibration*, vol. 17, no. 3, p. 4, 1998.

[33] O. Sigmund and J. Petersson, "Numerical instabilities in topology optimization: a survey on procedures dealing with checkerboards, mesh-dependencies and local minima," *Structural Optimization*, vol. 16, no. 1, pp. 68–75, 1998.

[34] K. Svanberg, "A class of globally convergent optimization methods based on conservative convex separable approximations," *SIAM Journal on Optimization*, vol. 12, no. 2, pp. 555–573, 2002.

[35] B. R. Sher and R. A. S. Moreira, "Dimensionless analysis of constrained damping treatments," *Composite Structures*, vol. 99, pp. 241–254, 2013.